Analytical Modeling of Industrial Related Silicon Solar Cells

Tobias Fellmeth, Florian Clement, and Daniel Biro

Abstract—**Fast and accurate simulation tools are key in increasing our understanding of silicon based solar cells. A lucid graphical unit interface and experimentally obtained input parameters help make these tools accessible for a wide range of users. In this work, we present a fast Excel tool based on the well-known two-diode-model supporting conventional and metal wrap-through cell architectures. The selective emitter approach, spatial varying emitter recombination and optical simulations are taken into account. A set of consistent input parameters including the emitter recombination in the passivated case, as well as the metal-contacted for both idealities are given as a function of the emitter sheet resistance. This set on input parameters is associated to industrial related technologies for conventional and metal wrap-through silicon solar cells.**

Index Terms—**Modeling, Solar cell, MWT, Emitter**

I. Introduction

SIMULATION of silicon solar cells is of key importance for the whole photovoltaic industry. The different approaches can be classified into three different approaches, which differ in the degree of complexity.

The first approach uses two and three dimensional device simulations with software tools like Sentaurus [1], ATLAS [2] or Comsol [3]. A symmetric element of the device is defined and meshed in finite elements. Boundary conditions for the differential equations for holes and electrons lead to a convergent solution on these elements. Since this approach is based on fundamental device physics using the transport and continuity equations, the highest degree of accuracy can be expected. However, inherently dealing with such complex software consumes computer and labor time.

The second approach uses three-dimensional or pseudo three dimensional network simulations. In the software tool SPICE [4] a mesh needs to be defined in which local diodes are linked with resistors. The physics of the minority charge carriers are described in the two-diode model by the dark saturation current densities j_{01} and j_{02}[1] for each node. Within this approach, the spatial characteristics of a solar cell are still represented accurately in the simulation, yet the overall simulation procedure is less complex. Since the two-diode model is used, ray tracing is not necessary and no differential equations describing the minority charge carrier transport need to be solved, thus, reducing the complexity of the simulation procedure. However, resistive effects caused by the majority charge carriers are still of the distributed kind and must be modeled in accordance to the Kirchhoff rules leading also to differential equations.

The last approach is referred to zero or one-dimensional modeling by using one global two-diode-model with a lumped series resistance for the whole device. This approach leads to the approximation of a spatial constant junction voltage V_j that in turn leads to a spatial constant series resistance that only depends on device geometry and electrical properties such as metal resistivity or emitter sheet resistance. Computing time of such an approach lies in the range of seconds.

In this paper the authors present an Excel based tool named Gridmaster, for silicon solar cells using the third approach described above. The tool optimizes the front metal grid pattern of conventional solar cells exhibiting the "H-grid" pattern as well as back contact metal wrap-through MWT [5] solar cells. The following features are included:

1. The two-diode model
2. Graphical unit interface
3. Selective emitter structures
4. Recombination at emitter/metal interfaces
5. Modeling of concentrator solar cells

II. The Excel Tool Gridmaster

A. Basic work principle

There is a fundamental trade-off between light shading and electrical resistance in a solar cell with a metal grid on the light facing, or front side. Two quantities describe this trade off.

1. The photo generated current j_{ph}, that reaches its maximum when the metal coverage fraction F_M equals zero
2. The series resistance r_s of the whole solar cell device that describes heat dissipation at an ohmic resistor, which reaches its maximum when F_M equals zero

Tobias Fellmeth, Florian Clement, and Daniel Biro are with the Fraunhofer Institute for Solar Energy Systems ISE, Freiburg, Germany. Corresponding Author: Tobias Fellmeth, phone: +49 761 4588 5596; e-mail: tobias.fellmeth@ise.fhg.de.

[1] Variables using a "*j*" are always current densities and from now on will be denoted as currents only.

Therefore, a parameter needs to be found that relates F_M to r_s and j_{ph}.

The front side[2] electrode of a conventional solar cell is based on a so-called “H-pattern”, which exhibits a parallel grid finger structure perpendicular to the broad busbars. Thus, the quantity of the screen-printed grid fingers n_f relates to $j_{ph} = j_{ph}(n_f)$ and $r_s = r_s(n_f)$ and therefore to the conversion efficiency η of the solar cell device. A typical graph exhibiting an optimum is shown in Fig 1.

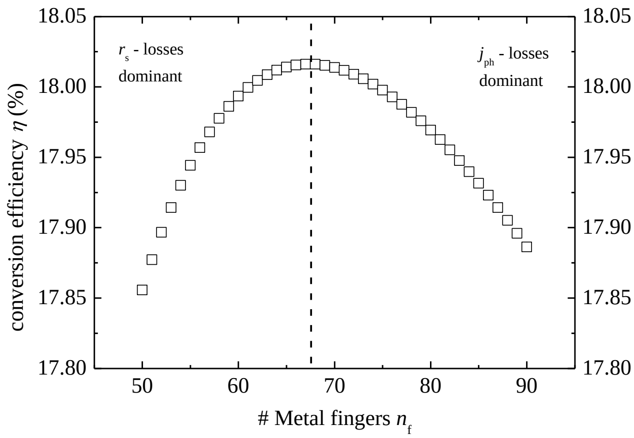

Fig 1 n_f is a variable of j_{ph} and r_s which both affects the maximum power output of a solar cell device. Therefore, the conversion efficiency η is linked to n_f and reaches a maximum.

Due to the p-n-junction of a solar cell the current-voltage-characteristic follows an exponential law given by Shockley in 1949 [6]. During operation, the voltage at the p-n-junction V_j is increased compared to the voltage between the external contact V due to the series resistance. Hence, the external voltage generated from the solar cell V in Shockley’s diode equation reads[3] $V_j = V - r_s\, j$.

A deviation of the ideal diode characteristic was first mentioned by Sah et al. [7]. He pointed out that Shockley-Read-Hall recombination [8] induced by mid-gap defect states in the space charge region exhibit an ideality factor of two. Therefore at low voltage forward bias, the current-voltage-characteristic can be mainly dominated by a diode with an ideality factor of $n = 2$. Finally, the two-diode-model for an illuminated solar cell reads:

$$j = j_{01} \cdot \left(e^{\frac{V - r_s \cdot j}{V_t}} - 1 \right) + j_{02} \cdot \left(e^{\frac{V - r_s \cdot j}{2 \cdot V_t}} - 1 \right) + \frac{V - r_s \cdot j}{r_p} - j_{ph} \qquad (1)$$

where V is the voltage generated between the external metal contacts, V_t the thermal voltage, r_p the area weighted parallel resistance, $j_{01} = j_{01}(n_f)$ the global dark saturation current with an ideality factor of one and $j_{02} = j_{02}(n_f)$ the global dark saturation-current with a ideality factor of two. The dark saturation-currents can also depend on n_f when recombination is accounted for at the emitter-metal interface (j_{01}) and the space charge region underneath (j_{02}) respectively [9-12]. The equivalent circuit corresponding to the two-diode-model is displayed in Fig 2.

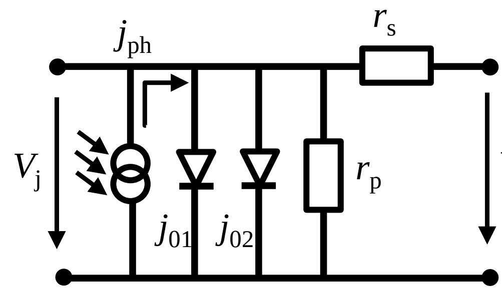

Fig 2 An equivalent circuit diagram shows the two-diode-model as implemented in Gridmaster. Two diodes with an ideality factor of $n = 1$ and $n = 2$ are incorporated.

At given n_f, the input parameters for equation 1 are calculated as described later in the paper. The resulting IV-curve yields the short-circuit-current j_{sc}, the open-circuit-voltage V_{oc}, the fill factor FF and the conversion efficiency η. By variation of n_f a graph as shown in Fig 1 is generated where in this case, an optimal balance between resistive, shading and recombination losses is found at $n_f = 67$. In Fig 3, the flow chart visualizes the operating principle of the Excel based tool “Gridmaster”.

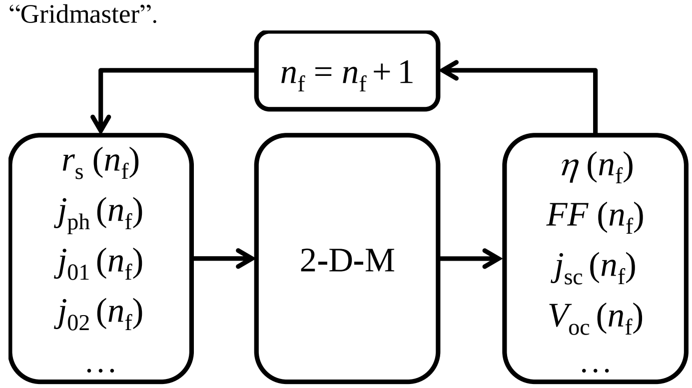

Fig 3 Flow chart of the Excel based software tool Gridmaster. j_{01} and j_{02} are the dark saturation currents from the diodes displayed in Fig 2. The lower and upper bound of n_f is defined priory resulting in a graph as displayed in Fig 1.

B. Calculating the total series resistance r_s

Every solar cell with a metal grid on one or both sides and a full area emitter has at least four inherent contributions to the total series resistance r_s [13, 14]. These are:

1. r_B: current flow of charge carriers in the bulk
2. r_E: lateral flow of charge carriers in the emitter
3. r_c: contact resistance at the emitter-metal interface
4. r_f: electron flow in the metal electrodes (grid)

It is common to distinguish between a series resistance that is generated from the front side r_{s_front} (emitter and metallization) which depend on n_f and from the bulk and rear side r_{s_rear} independently from n_f.

r_B and r_E occur within the semi-conductor material and can

[2] Corresponds always to the illuminated side of the solar cell.
[3] In this case, the forward biased IV-curve is in the fourth quadrant, so $j < 0$ for $V < V_{oc}$ and $r_s\, j$ needs to be subtracted from V. The sign in the exponent originates from the junction voltage V_j being higher compared to the external voltage V under illumination.

depend on the injection level. A constant expression can only be found if the approximation of low level injection holds at least up to the maximum power point voltage V_{mpp}. Usually, for industrial p-type solar cells this condition is fulfilled [15].

Further contributions to the series resistance have to be taken into account, if the front busbars and the rear aluminum are contacted locally leading additionally to r_{BB} and r_{Al} respectively. The transition resistance between the highly doped back surface field and the eutectic Al-layer on the rear side can be neglected.

The MWT solar cell enables a higher conversion efficiency potential compared to the conventional H-grid design [16] although it exhibits additional contributions to r_s [17]. These contributions are:

- Lateral current flow over the rear n-contact pads in the bulk r_L
- Current flow through the metal filled vias from the front to the rear side r_{via}

In the MWT case, resistive losses occur in continuous metallic n-pads on the rear side and depend on the number of external contact pins. However, recent designs for the rear side of MWT solar cells have local pads [18, 19]. In this case, each pad is externally contacted and lateral current flow in the metal is suppressed effectively. Hence, the contribution to the total series resistance can be neglected ($r_{BB} \sim 0$).

The derivation of r_s and its implementation in "Gridmaster" is shown in the appendix.

C. Implementation of the selective emitter approach

The selective emitter approach [20] combines a highly n^{++} doped emitter underneath the front electrode and in the illuminated area a weaker doped emitter n^{+}. This enables simultaneously, a low contact resistance of the front electrode and a reduced Auger-recombination in the n^{+}-emitter leading to a higher j_{sc} and V_{oc} potential.

The increased repelling of minority charge carriers from reaching the emitter-metal interface is a frequently underestimated effect of a selective emitter [21]. This effect is reflected in the dark saturation currents $j_{0e\text{-met}}$ and $j_{02\text{-met}}$. The former complies with a diode ideality factor of $n = 1$ and the latter of $n = 2$. By area weighting the local dark saturation currents that share the same ideality factor the effective dark saturation currents j_{01} and j_{02} are obtained [22]. Therefore, the global dark saturation current introduced in Fig 2 in case of a diode with an ideality factor of $n = 1$ reads:

$$j_{01} = j_{0b} + (1 - F_{n^{++}}) \cdot j_{0e-n^{+}} + (F_{n^{++}} - F_M) \cdot j_{0e-n^{++}} + F_M \cdot j_{0e-met} \quad (2)$$

And for the diode with an ideality factor of $n = 2$ following expression holds:

$$j_{02} = (1 - F_M) \cdot j_{02-n} + F_M \cdot j_{02-met} \quad (3)$$

j_{0b} denotes the dark saturation current of the bulk and the rear side, $j_{0e\text{-n+(+)}}$ the dark saturation currents of the weakly and highly doped emitter respectively, $j_{0e(02)\text{-met}}$ the dark saturation currents of the metallized emitter, $j_{02\text{-n}}$ the dark saturation current of the passivated emitter for the assumption that n^{+} and n^{++} share the same j_{02}, F the area fraction of the regarded j_0.

The area-weighted addition of j_0 values requires a negligible variation of access charge carriers Δn between neighboring regions. A recent study from Greulich et al. [22] supports this approach for emitters with sheet resistances between 11 and 120 Ω/sq under standard test conditions.

Fig 4 displays a cross-section of a front grid finger contacting the selectively phosphorus doped emitter. Although the metal electrode partly shades the n^{++}-area in this case, the dark saturation current is, by definition, unaffected by illumination. Hence $j_{0e\text{-n++}}$ is constant throughout the non-contacted shaded part of the solar cell device. The j_{02}-value is assumed to be constant for the case of a passivated emitter. In Section III-C, of this paper, this assumption is discussed in more detail.

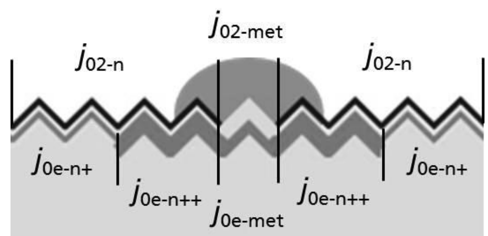

Fig 4 A schematic cross-section of a device featuring a selective emitter is shown that exhibits three areas represented by its dark saturation currents. In this case, a seed-layer provides the emitter-metal contact and subsequent silver or copper plating step generates the bulk finger.

III. Input Parameters

For exact modeling, precisely measured input parameters are a mandatory requirement. In this chapter, a set of input parameters for "Gridmaster" are identified and presented. To this purpose, 2 x 2 cm² sized, FZ-Si based solar cells with printed front grid have been fabricated. A wafer featuring eight individual solar cells is shown in Fig 5.

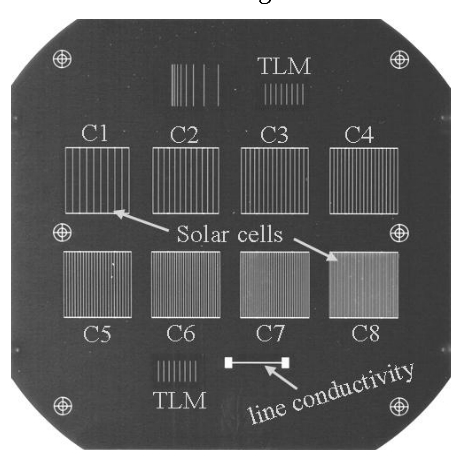

Fig 5 The front view of a whole 5'' wafer is displayed. Eight individual solar cells are realized on one wafer (C1-C8). Additionally, support structures for characterization are incorporated.

The cells feature a screen-printed metallization on both sides resulting in a full area aluminum back surface field (BSF) on the rear surface. The emitter is generated by means of a thermal diffusion in a tube furnace. In order to reduce edge effects, the perimeter of each cell is embedded in a so-called emitter-window.

A. Emitter recombination

A method to determine the value of $j_{0e\text{-met}}$ without the need of parallel processed lifetime samples has been published at the 1st SiliconPV [23]. The main idea features the determination of V_{oc} on actual solar cells with varying metallization fraction as shown in Fig 5. This value is sensitive to the emitter doping profile and front metallization and therefore to contact firing or annealing conditions.

For the passivated, $j_{0e\text{-n+}}$ values, the common method for symmetrically processed lifetime samples introduced by Kane and Swanson [24] has been applied.

The implementation of the experimentally obtained dark saturation currents in Gridmaster results in a parameterization over the emitter sheet resistance R_{sh} according to Fig 6.

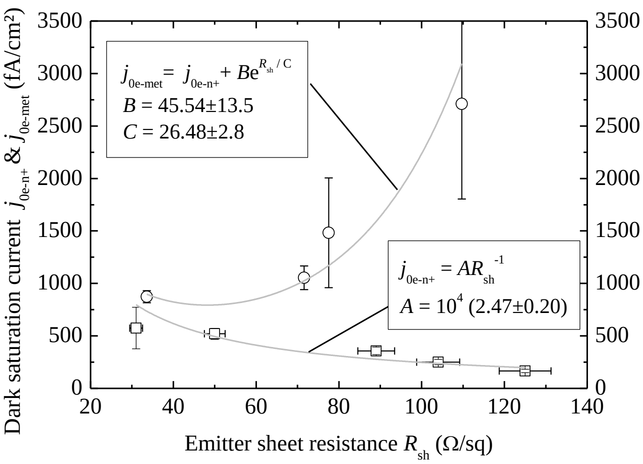

Fig 6 The recombination currents for the metallized emitter $j_{0e\text{-met}}$ and for the illuminated $j_{0e\text{-n+}}$ are displayed. We fit the data to extract a dynamic model in dependence of the emitter sheet resistance R_{sh}.

The trends of the fitted curves are in good accordance to the existing theory [9-11] and can be explained by shifting regimes between volume and surface recombination in the highly doped region. The fit functions are chosen based on the physical behavior. In the passivated case, $j_{0e\text{-n+}}$ vanishes for large R_{sh}. In the metallized case for low R_{sh}, the passivated and unpassivated converges and $j_{0e\text{-met}}$ corresponds $j_{0e\text{-n+}}$. For high R_{sh}, the resulting $j_{0e\text{-met}}$-value is dominated by the exponential term due to surface recombination at the emitter-metal interface.

Strictly speaking, the results presented in Fig 6 are only valid for one screen-printed thick-film paste and emitter doping profile. Based on experience, however, we know that other thick-film pastes fired on optimal conditions reach similar values of $j_{0e\text{-met}}$ on the respective emitter.

B. Recombination in the bulk and at the rear side

In the case of highly doped regions existing in a solar cell device, it is common practice to describe recombination that exists in this region in form of an effective surface recombination velocity S_{eff} or better in a characteristic dark saturation current j_0 independent of the bulk doping [25]. In case of a full area aluminum alloyed rear side, a guideline to extract j_0 can be found here [26].

The effective dark saturation current of the bulk and the rear side j_{0b} is obtained by linking recombination in the bulk and the rear side by means of a geometry factor G [25]:

$$j_{0b} = \frac{qDn_i^2}{N_A L_{Bulk}} \cdot \underbrace{\frac{\frac{S_{eff} \cdot L_{bulk}}{D} + \tanh\left(\frac{W}{L_{bulk}}\right)}{1 + \frac{S_{eff} \cdot L_{bulk}}{D} \cdot \tanh\left(\frac{W}{L_{bulk}}\right)}}_{G^{-1}} \tag{4}$$

Whereby, q denotes the elementary charge, D the diffusion coefficient of the minority carriers in the bulk, n_i the intrinsic charge carrier density in the bulk, N_A the acceptor density in the bulk, L_{bulk} the diffusion length in the bulk and W the thickness of the bulk.

In Fig 7, typical j_{0b} values for p-type silicon based solar cells for typical effective dark saturation currents at the rear j_{rear} are shown.

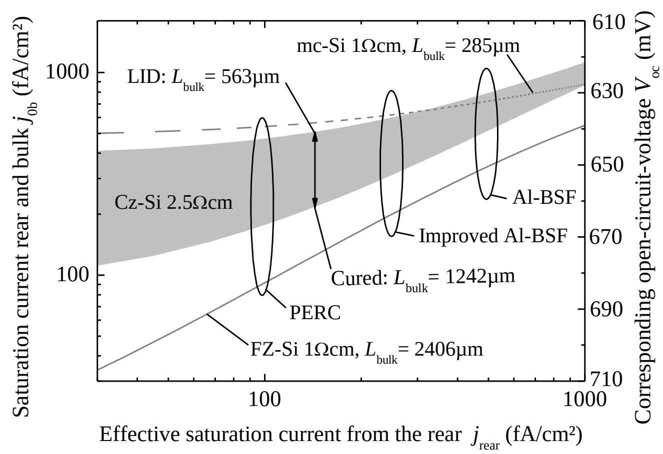

Fig 7 The saturation current of the rear and the bulk j_{0b} in dependence of the saturation current of the rear j_{rear} is shown. Typical bulk lifetimes for silicon and doping densities are incorporated. For Cz-Si, light induced degraded (LID) lifetime according to Bothe et al. [27] and a "cured" value of τ = 400 µs is used

However, the corresponding areas only serve as guidelines, since they depend on technological aspects and surface preparation of the bulk material incorporated.

C. Non-ideal recombination

The expression "non-ideal recombination" combines recombination mechanisms that lead to ideality factors greater than one. This generates a kink [28] visible in the logarithmic plotted dark I-V or suns-V_{oc}-curve [29] which, in most cases, influences the maximum power point of a solar cell device.

In order to model losses associated to non-ideal recombination, the quantity j_{02} has been introduced by Sah [7] and Nussbaum [30]. They derived an ideality factor of $n = 2$

by assuming a single mid-gap defect state associated to a contamination of the silicon material. The authors assume a penetration of impurities during contact sintering through the emitter layer to the depletion region. Following procedure for the determination of j_{02} has been used:

1. Calculation of j_{01} out of the quantities $j_{0e\text{-}n+}$ and $j_{0e\text{-}met}$, priory determined in Section III-A in this paper
2. Generation of the IV-curve by means of the one-diode-model
3. Addition of the second exponential term associated to j_{02} with a constant ideality factor of n = 2until the corresponding fill factor matches the measured suns-V_{oc} fill factor *pFF*

The advantage of the present model corresponds to its simplicity ignoring physical effects that might increase the ideality factor to two or beyond [28], [31-34]. The fill factor losses are regarded as effective quantities in the values j_{02} and $j_{02\text{-met}}$. Note: this analysis has been conducted for negligible shunt current. At present shunt, the leakage current at maximum power point needs to be considered additionally.

Due to the chosen approach, the authors assume a constant j_{02} for effectively passivated emitter regions leading to $j_{02} = j_{02\text{-}n+} = j_{02\text{-}n++}$.

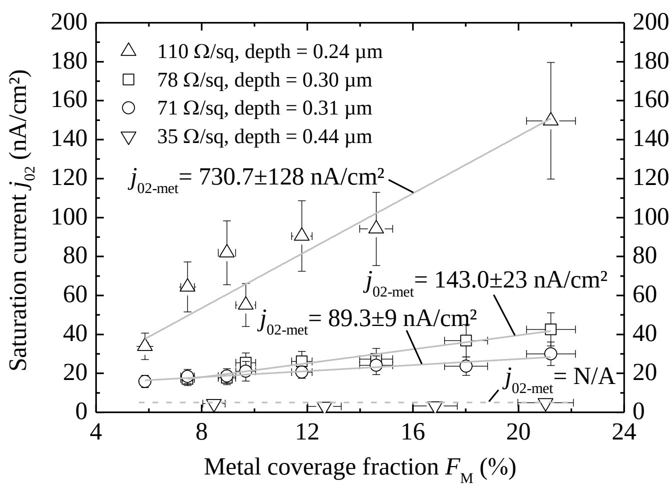

Fig 8 The recombination current j_{02} is plotted in dependence of the metal coverage for different emitter sheet resistances. The depth of the profile corresponds to a doping level of 10^{17} cm^{-3}

In Fig 8, the effective saturation current j_{02} is plotted versus the metal coverage fraction F_M on different emitters. As can be seen in the figure, j_{02} scales with the emitter sheet resistance and thus with the depths of the emitter corresponding to the location of the depletion region. In order to separate the influence of the emitter-metal contact on j_{02} from other influencing quantities, the expression $j_{02\text{-met}}$ is introduced in Equation 3.

The emitter with a sheet resistance of 35 Ω/sq shows hardly any significant slope, thus a disappearing $j_{02\text{-met}}$.

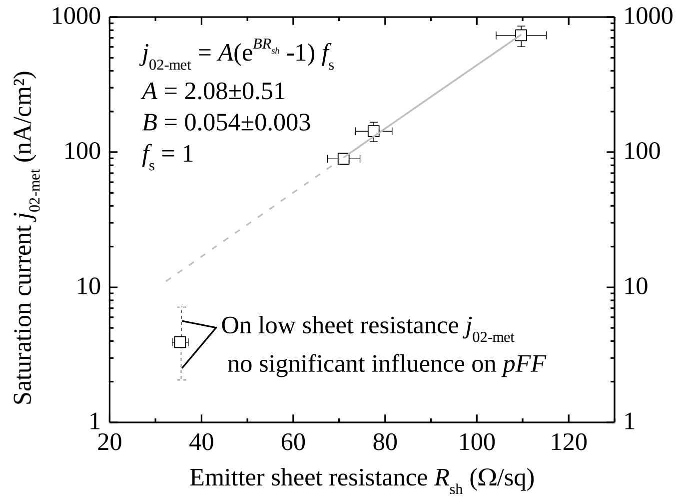

Fig 9 The extracted $j_{02\text{-met}}$ is plotted versus the corresponding emitter sheet resistance. The value for the 35 Ω/sq emitter is obtained by averaging values given in Fig 8. It shall demonstrate the strong decrease of $j_{02\text{-met}}$ with decreasing emitter sheet resistance. Therefore, the extracted fit-function indicated by the dashed line serves as upper bound. The factor f_s enables a scaling of the resulting parameterization of $j_{02\text{-met}}$.

Fitting the values extracted with Equation 3, relates $j_{02\text{-met}}$ to the emitter sheet resistance and leads to an empirical model shown in Fig 9. The strong influence of R_{sh} on $j_{02\text{-met}}$ supports the approach of the contaminated depletion region by the front electrode. In case of nickel seed-layer approaches, this behavior is already known [35].

Please note that the obtained parameterization of $j_{02\text{-met}}$ is influenced by the fixed ideality factor of n = 2. In addition, it is likely that due to mentioned effects a voltage independent n or j_0 cannot always be found. Furthermore, we observe a strong dependence of the firing temperature and chosen paste on *pFF*. Therefore, we introduce a scaling factor f_s, that is initially set to f_s = 1 and accounts for the strong diversity and dependencies of this parameter. A more detailed analysis regarding paste and temperature dependence is published by Hoenig et al.[12].

D. Photo generated current

The so called "blue-response" is strongly influenced by the amount of phosphorus incorporated in the front highly doped region [36]. In order to obtain an analytical model, we relate the emitter sheet resistance to the photo generated current as demonstrated in Fig 10. A dead-layer model introduced in Fischer's Ph.D. thesis [37] enables the separation of emitter and bulk losses in the internal quantum efficiency. This model has been implemented by Thaidigsmann et al. [38] and experimentally verified by Jäger et al. [39].

The upper curves in Fig 10 show the limit in photo-generated current in dependence of R_{sh} for two different rear side concepts.

As can be seen, the photo-generated loss in the emitter region is inversely proportional to the emitter sheet resistance. In case of a full area Al-BSF, the maximum photo-generated current reaches 40 mA/cm². However, for a PERC device with superior rear properties the limit reaches 41.5 mA/cm². These values strongly depend on cell thickness and optical properties of both front and rear side and therefore have to be determined individually. These limits have been obtained by applying an analytical model presented in [37], taking into account carrier lifetime, thickness and optical properties of the bulk and rear. Free carrier absorption of near band gap light in the emitter region is not taken into account here. An additional implementation is doable and can be found in [40].

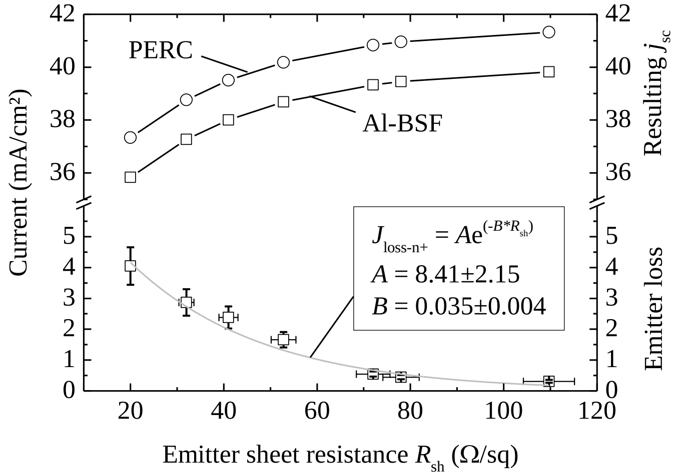

Fig 10 The experimentally obtained loss in photo generated current due to emitter recombination in dependence of the emitter sheet resistance in the lower section of the graph is displayed. For the solar cell with a full area Al-BSF, the maximum photo generated current is limited at 40 mA/cm², however, for a PERC device with superior rear reflectance the limit reaches 41.5 mA/cm².

IV. Results

Using the parameter set presented in Section III in "Gridmaster", very good agreement is obtained between the measured and the simulated data. The measured IV data for the solar cell device presented in Section III is shown in Fig 11 and Fig 12. The V_{oc} decreases due to the increased area of the unpassivated emitter and decreasing j_{sc}. Publications from Cuevas et al. [41] and Greulich et al. [42] report decreasing V_{oc}, with increasing influence of resistive losses. The effect is related to the distributed series resistance of a solar cell and enhanced by high $j_{0e\text{-}met}$ values. It seems for 10 or lower grid fingers this behavior is on setting. However, for solar cells with a typical series resistance of around 1 Ωcm² or less, this effect is of minor magnitude.

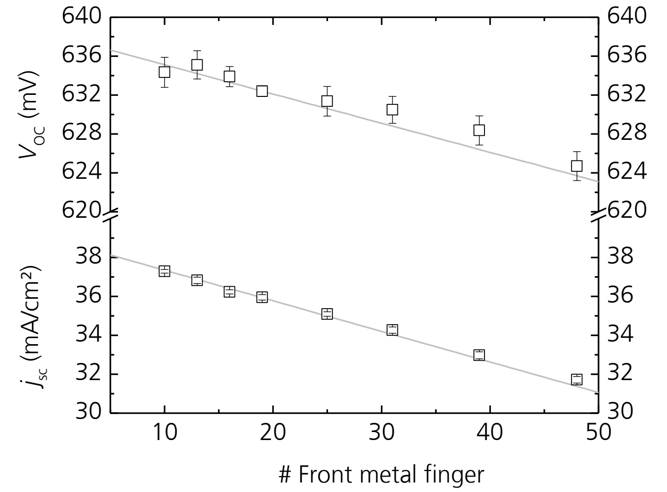

Fig 11 The open-circuit-voltage V_{oc} and the short-circuit-current j_{sc} measured and simulated are shown. The median value from six solar cells corresponds to one data point.

As can be seen, measured and simulated efficiency are in good accordance.

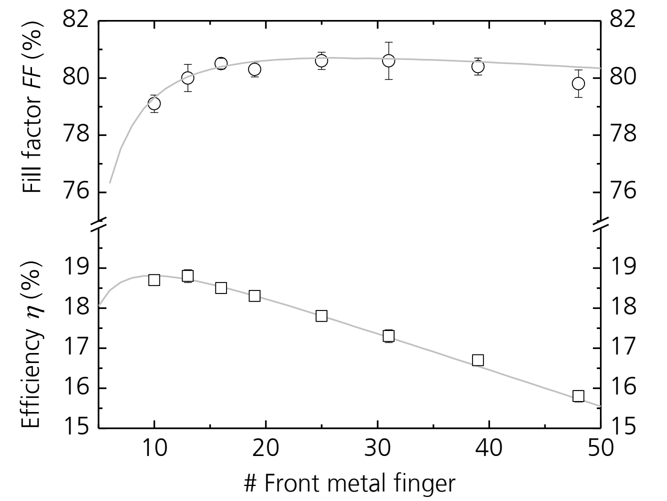

Fig 12 The fill factor FF and the conversion efficiency η measured and simulated are shown. The median value from six solar cells corresponds to one data point.

Additionally, in Table 1 further input parameters are displayed. An effective finger height refers to a rectangle with the same cross-sectional area compared to the original shape.

Table 1 In addition to the parameters presented in section III, further experimentally obtained parameters are utilized. The effective finger height has been obtained as quotient of the cross-sectional area and the finger width. The contact resistivity is measured by means of the TLM approach [43].

Solar cell	2 x 2 cm², Si-FZ
Effective finger height	9.1 µm
Finger width	85 µm
Busbar width	197 µm
Paste resistivity	5 µΩcm
Emitter sheet resistance	71 Ω/sq
Contact resistivity	3.3 Ωcm²

V. Conclusion

In this work, an Excel based analytical tool named Gridmaster is presented allowing the fast analytical modeling of conventional and metal wrap-through solar cells.

A detailed characterization relates important input parameters required for the simulation of conventional and metal wrap-through solar cells to the emitter sheet resistance. Those parameters are: the dark saturation current of the passivated and metallized emitter area, non-ideal recombination expressed as an effective dark saturation current with an ideality factor of two and the photo generated current for full area alloyed Al and PERC devices.

As a remarkable result is the distinguished correlation between sheet resistance and non-ideal recombination. It has been experimentally shown that solar cells with a lowly doped emitter under the front electrode exhibit an increased recombination, which affects both the open circuit voltage and the fill factor. Both loss mechanisms are expressed in the dark saturation current densities $j_{0e\text{-met}}$ and $j_{02\text{-met}}$. Regarding the latter, the authors show the impact of a metal contaminated depletion region for a sintered front electrode. This quantity is strongly related to the emitter profile, the screen-printing paste and sintering conditions and has to be considered individually.

Appendix

The series resistance in conventional solar cells

The “lumped series resistance” approach for modeling the power drop due to resistive losses is well known and described in the standard references [13, 14]. The idea is based on the reduction of the device to its smallest periodical structure – the elementary or unit cell. Due to the periodicity, physical properties in one single unit are extendable to the whole device. In Fig 13, one of the possible unit cell designs are emphasized. It enfolds half of the BB-BB distance including one grid finger and a BB segment.

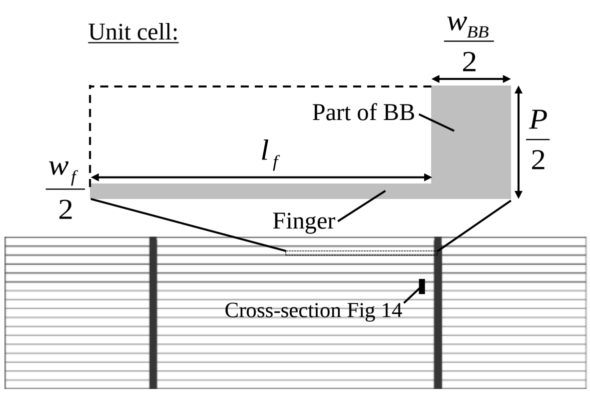

Fig 13 A typical front grid of a conventional solar cell is displayed. Enlarged is one possible unit cell for this kind of grid structure.

A. The series resistance of the emitter

During operation under illumination, electrons are assumed to be injected homogenously in the emitter. Therefore, the electron flow in the unit cell increases linearly towards the edge of a grid finger. This assumption leads to following expression for the series resistance caused by the emitter:

$$r_E = \frac{1}{6} \cdot R_{Sh} \cdot \frac{(P - w_f)}{l_f} \cdot A_{EZ-I}, \quad A_{EZ-I} = \frac{P}{2} \cdot \left(l_f + \frac{w_{BB}}{2} \right) \tag{5}$$

Whereby, R_{sh} is the sheet resistance of the emitter. This expression neglects electrons that are collected by the busbar.

In order to account for a selective emitter, the expression for the series resistance needs to be extended to account for the current flow through the highly doped emitter area n^{++}.

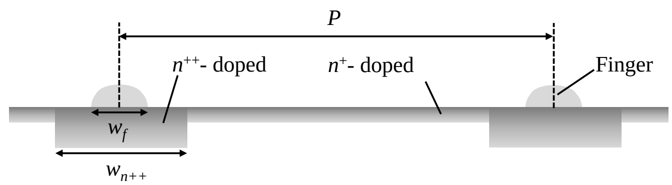

Fig 14 A cross-section as indicated in Fig 13 is shown.

According to the cross-section indicated in Fig 13 and Fig 14, the expression for the lowly doped part reads:

$$r_{E-n^+} = \frac{1}{6} \cdot R_{Sh-n^+} \cdot \frac{(P - w_{n^{++}})}{l_f} \cdot A_{EZ-I} \tag{6}$$

For the highly doped region, a more complex equation is obtained. The power loss PW in this area reads:

$$PW_{E-n^{++}} = \frac{1}{3} \cdot \frac{R_{Sh-n^{++}}}{j_{ph-n^{++}} \cdot l_f^{\,2}} \cdot \left(\left(I_{ph-n+} + j_{ph-n^{++}} \cdot \frac{l_f}{2} \cdot (w_{n^{++}} - w_f) \right)^3 - I_{ph-n^+}^{\;3} \right) \tag{7}$$

An expression for the series resistance is obtained by dividing (7) with the square of the maximum current I_{max}^2 flowing through the highly doped emitter.

$$r_{E-n^{++}} = \frac{PW_{E-n^{++}}}{I_{max}^{\;2}} A_{EZ-I} \quad I_{max} = j_{ph-n^+} \cdot \frac{l_f}{2} \cdot (P - w_{n^{++}}) + j_{ph-n^{++}} \cdot \frac{l_f}{2} \cdot (w_{n^{++}} - w_f) \tag{8}$$

Contrary to the lowly doped case, this expression depends on the currents generated throughout the whole emitter area. In order to obtain an analytical equation, the apparent external current $j(V)$ is substituted by the photo generated currents $j_{ph\text{-}n+(+)}$. This approach leads to a small overestimation of the series resistance in the n^{++}-emitter.

B. The series resistance of the front metal grid

Along the grid finger toward the busbar the electron flow increases linearly, so the expression for the series resistance in the grid finger reads:

$$r_f = \frac{2}{3} \cdot \rho_f \cdot \frac{l_f}{w_f \cdot h_{f\_eff}} \cdot A_{EZ-I} \tag{9}$$

Whereby, ρ_f represents the specific resistance of the grid fingers and h_{f_eff} the effective height corresponding to a grid finger with a rectangular cross-section.

Losses due to current flow in the busbar depend on the external contact geometry. Usually, an array of pin-pairs is utilized for current and voltage contacting each busbar homogenously. Therefore, the expression for the series resistance occurring in the busbar reads:

$$r_{BB} = \frac{1}{3} \cdot \rho_{BB} \cdot \frac{w_c}{2 \cdot n_{Pins-BB} \cdot h_{BB} \cdot w_{BB}} \cdot A_{EZ-II}, \quad A_{EZ-II} = \frac{w_c \cdot l_c}{2 \cdot n_{Pins-BB} \cdot n_{BB}} \tag{10}$$

Whereby b_c/l_c is the width/length-ratio of the whole cell, h_{bb}/w_{BB} is the height/width-ratio of the busbar, $n_{\text{Pins-BB}}$ is the quantity of current pins contacting one busbar and n_{BB} is the quantity of busbars.

It is assumed that half of the current pin-to-pin distance along the busbar is much larger than the grid finger pitch.

C. The contact resistance of the silicon-metal interface

For the contact resistance the following expression is used:

$$r_c = \frac{\rho_c}{\left(\left(l_f + \frac{1}{2}\left(P - w_f\right)\right) \cdot L_T\right)} \cdot \coth\left(\frac{w_f}{2 \cdot L_T}\right) \cdot A_{EZ-I}, \quad L_T = \sqrt{\frac{\rho_c}{R_{sh-n^{+(+)}}}} \tag{11}$$

Whereby, ρ_c is the specific contact resistance and L_T is the transfer length. Due to the non-linear hyperbolic cotangent in (11), the choice of the unit cell is restricted to the size as defined in (5). Furthermore, l_f is extended by P in order to take into account current collection by the busbar that slightly reduces the resulting contact resistance.

D. The series resistance of the bulk

For the expression of the series resistance in the bulk, it is assumed that photo generation exists only at the front side. Therefore, all holes reaching the rear side propagate through the total thickness of the device. Hence following equation for the series resistance in the bulk holds for the upper limit:

$$r_B = \rho_B \cdot W \tag{12}$$

Whereby, ρ_B is the specific resistivity of the bulk silicon and W the thickness of the device.

E. The series resistance of the rear electrode

The current flow through the rear electrode depends on the external contact geometry. In the most cases, the external contact of the fully metallized rear side is realized by an array of pins opposing the array contacting the front n-contact. Therefore, the following assumption holds $n_{\text{BB-front}} = n_{\text{Pad-rear}} = n_{BB}$. In order to account for the two dimensional current flow, an approach commonly used for the front side of EWT [44] solar cells is taken.

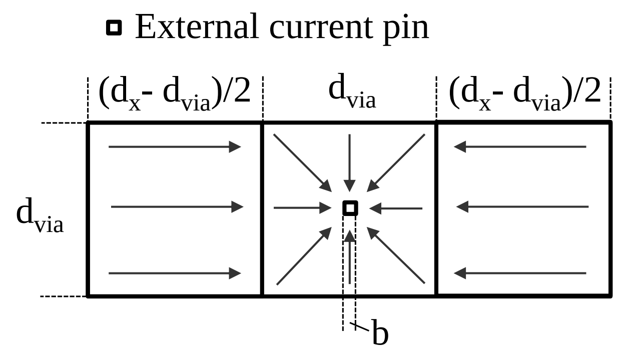

Fig 15 The idealized current flow pattern within a unit cell of the rear side towards an external current pin is displayed. The unit cell is divided in two areas, a rectangular shaped (“rec”) region where current is assumed to flow in parallel and a square region (“sq”) located around the external current pin where radial current flow is assumed.

In this section, all following equation are based on Hall and Solty [45] and has been extended by Fallisch et al. [46].

$$r_{sq} = \cdot \frac{R_{Sh-Al} \cdot d_{via}^{\,2}}{2 \cdot \pi} \cdot \left(\ln\left(\frac{d_{via}}{b}\right) - \frac{3}{4} + \frac{b^2}{d_{via}^{\,2}} - \frac{b^4}{4 d_{via}^{\,4}}\right) \cdot \left(1 + \frac{d_x - d_{via}}{d_{via}} f\right) \tag{13}$$

Equation 13 takes into account a radially symmetric current flow pattern within the square around the external current pin and introduces correction factors for compensation of deviations from radial symmetry. The empiric factor f compensates for the current flowing only through two sides of the square. The assumed current flow pattern is shown in Fig 15.

The following equation is taking into account parallel current flow in the rectangular part of the unit cell. This equation has been modified compared to its literature form in order to maintain monotonous decreasing behavior of equation (15) towards vanishing d_{via}.

$$r_{rec} = \frac{1}{12} \cdot R_{sh-Al} \cdot d_x^{\,2} \tag{14}$$

Finally, equation 15 yields the losses associated to the current flow through the rear metallization of a solar cell.

$$r_{s-Al} = r_{sq} + r_{rec} \tag{15}$$

Fig 16 displays the series resistance for the rear metallization according to (15). For $d_{\text{via}} = 0$ ($n_{\text{pin-Al}} = \text{inf.}$), equation 13 vanishes and $r_{\text{s-Al}} = r_{\text{rec}}$

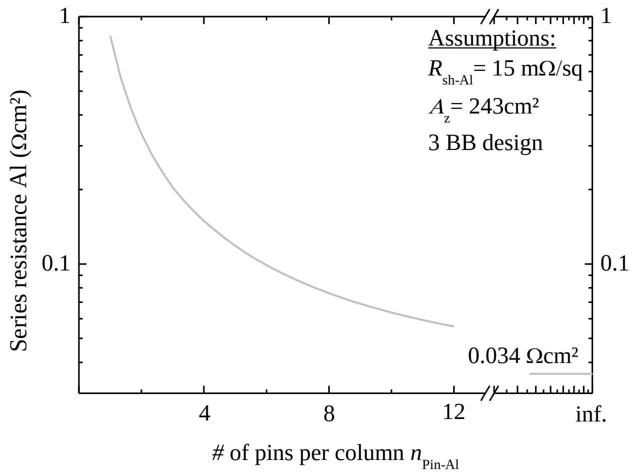

Fig 16 Series resistance according to (15) is displayed. For vanishing d_{via} ($n_{pin\text{-}Al}$ = inf.), (13) vanishes and (15) converges into (14).

MWT related losses

The metal wrap-through MWT approach enables a higher efficiency potential compared to the conventional solar cell architecture. In contrary, series resistance losses are more pronounced due to additional contributions [17].

A. The series resistance of the via through metallization

All vias (n_{via}) connect the front electrode to the rear pads in parallel. Therefore, by assuming a homogenous distribution of vias and an average via resistance R_{via}, the weighted contribution is obtained as follows.

$$r_{via} = \frac{R_{via}}{n_{via}} \cdot w_c \cdot l_c \tag{16}$$

B. The lateral series resistance of the bulk

A geometrically inspired approach leads so a simple analytical equation of the lateral series resistance in the bulk [17].

$$r_{Lat-cont} = \frac{1}{24} \cdot \rho_B \cdot \frac{w_{Al}^{3}}{W \cdot l_f} \tag{17}$$

Equation 17 assumes a continuous n-pad on the rear side as outlined in Fig 17 on the left side.

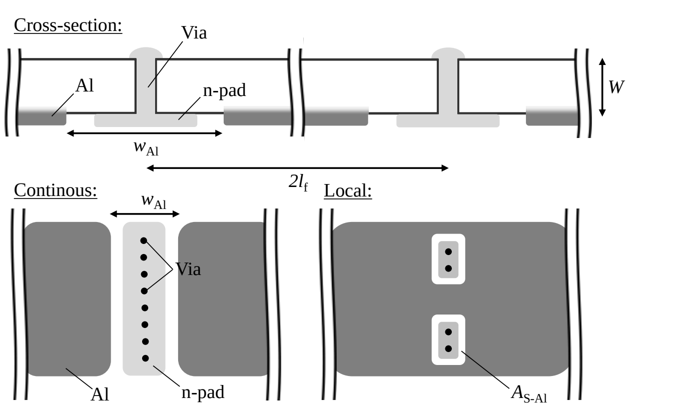

Fig 17 A cross-section, and two possible rear designs of a MWT solar cell are drawn.

In order to increase the coverage fraction of the electrically positive area, continuous n-pads are substituted by local structures as demonstrated in Fig 17 on the right side. Therefore, the area of the opening in the p-contact for one local n-pad is assumed to exhibit a radial symmetry with the radius R_o. Current flows radially from the origin of the circle toward the p-contact and increases linearly. Hence, the lateral series resistance $r_{Lat\text{-}Loc}$ induced by a local n-pad in respect to the standard “power-loss-approach” reads:

$$dPW_{Lat-Loc} = I^2 \cdot dR = \left(j\pi r_o^{\,2}\right)^2 \cdot \rho_B \frac{dr_o}{2\pi r_o W}$$

$$PW_{Lat-Loc} = \rho_B \frac{j^2 \pi}{2W} \cdot \int_0^{R_o} r_o^{\,3} dr_o = \rho_B \frac{j^2 \pi R_0^{\,4}}{8W}$$

$$R_{Lat-Loc} = \frac{P}{\left(j\pi R_o^{\,2}\right)^2} = \frac{\rho_B}{8\pi W}$$

$$r_{Lat-Loc} = R_{Lat-Loc} \cdot \underbrace{A_{s-Al}}_{EZ} \cdot \underbrace{\frac{A_{s-Al} \cdot n_{Loc}}{w_c \cdot l_c}}_{weighting} = \rho_B \cdot \frac{\pi R_o^{\,4}}{8W} \cdot \frac{n_{Loc}}{w_c \cdot l_c} \tag{18}$$

Whereby n_{Loc} is the total quantity of local n-pads on the rear side. Lateral current in the base due to solder p-pads is accounted for the same way. Note: The unit cell $A_{s\text{-}Al}$ is no periodic element of the solar cell. Therefore, its contribution to the lumped series resistance needs to be weighted with a periodic element that includes the chosen unit cell (equation 17 is obtained the same way).

Note: The solder pads providing the p-contact for both conventional and MWT solar cell might also induce an area of lateral current flow in the bulk and depending on geometry treated as defined in equation 17 or 18.

C. The series resistance in the rear n-pad

In the case of a continuous n-pad, current flows toward the next accessible external current pin providing the same loss as in a case of a front busbar. Therefore, Equation 10 holds if adapted to respective geometry and resistivity.

In case of local n-pads, current is transferred by the grid fingers to the pseudo-busbar on the front side of the MWT solar cell and is treated as a series resistance of a busbar on the front side.

ACKNOWLEDGMENT

The authors would like to thank Stefan Glunz, Dominic Huljić, Matthias Hörteis, Ansgar Mette for their pioneering involvement on the tool presented in this work, also Prof. Willeke and Prof. Clement for their fruitful discussion and finally the whole PV-TEC team for processing and characterization.

References

[1] Sentaurus TCAD, "release E-2010.12," ed. Zürich, Switzerland: Synopsys, 2010.

[2] Atlas, Atlas User Manual 2013, ed. Santa Clara, CA: Silvaco.

[3] K. Rapolu, P. Singh, and S. P. Shea, "Two dimensional numerical modeling of a silicon solar cell with deep contacts in the emitter," in *Proceedings of the 34th IEEE Photovoltaic Specialists Conference*, Philadelphia, Pennsylvania, USA, 2009, pp. 1048-53.

[4] L. W. Nagel and D. O. Pederson, "Simulation program with integrated circuit emphasis (SPICE)," in *Proceedings of the 16th Midwest Symposium on Circuit Theory*, Waterloo, Ont., Canada, 1973, pp. 1-65.

[5] E. van Kerschaver, R. Einhaus, J. Szlufcik, J. Nijs, and R. Mertens, "A novel silicon solar cell structure with both external polarity contacts on the back surface," in *Proceedings of the 2nd World Conference on Photovoltaic Energy Conversion*, Vienna, Austria, 1998, pp. 1479-82.

[6] W. Shockley, "The theory of p-n junctions in semiconductors and p-n junction transistors," *Bell System Tech. J.,* vol. 28, pp. 435-489, 1949.

[7] C. T. Sah, R. N. Noyce, and W. Shockley, "Carrier generation and recombination in p-n junctions and p-n junction characteristics," *Proceedings of the IRE*, vol. 45, pp. 1228-1243, 1957.

[8] W. Shockley and W. T. J. Read, "Statistics of the recombinations of holes and electrons," *Physical Review*, vol. 87, pp. 835-42, 1952.

[9] R. R. King, P. E. Gruenbaum, R. A. Sinton, and R. M. Swanson, "Passivated emitters in silicon solar cells," in *Proceedings of the 21st IEEE Photovoltaic Specialists Conference*, Kissimmee, Florida, USA, 1990, pp. 227-32.

[10] A. Cuevas, P. A. Basore, G. Giroult-Matlakowski, and C. Dubois, "Surface recombination velocity of highly doped n-type silicon," *Journal of Applied Physics*, vol. 80, pp. 3370-5, 1996.

[11] M. J. Kerr, J. Schmidt, A. Cuevas, and J. H. Bultman, "Surface recombination velocity of phosphorus-diffused silicon solar cell emitters passivated with plasma enhanced chemical vapor deposited silicon nitride and thermal silicon oxide," *Journal of Applied Physics*, vol. 89, pp. 3821-6, 2001.

[12] R. Hoenig, A. Kalio, J. Sigwarth, F. Clement, M. Glatthaar, J. Wilde, and D. Biro, "Impact of screen printing silver paste components on the space charge region recombination losses of industrial silicon solar cells," *Solar Energy Materials & Solar Cells,* vol. 106, pp. 7-10, 2012.

[13] A. Goetzberger, B. Voß, and J. Knobloch, *Sonnenenergie: Photovoltaik*. Stuttgart: Teubner Studienbücher Physik, 1994.

[14] M. A. Green, *Third Generation PhotovoltaicsAdvanced Solar Energy Conversion*, 2003.

[15] A. Cuevas and R. A. Sinton, "Detailed modelling of silicon solar cells," in *Proceedings of the 23rd European Photovoltaic Solar Energy Conference*, Valencia, Spain, 2008, pp. 315-9.

[16] F. Clement, M. Lutsch, T. Kubera, M. Kasemann, W. Kwapil, C. Harmel, N. Mingirulli, D. Erath, H. Wirth, D. Biro, and R. Preu, "Processing and comprehensive characterisation of screen-printed mc-si metal wrap through (mwt) solar cells," in *Proceedings of the 22nd European Photovoltaic Solar Energy Conference* Milan, Italy, 2007, pp. 1399-402.

[17] F. Clement, M. Menkoe, T. Kubera, C. Harmel, R. Hoenig, W. Wolke, H. Wirth, D. Biro, and R. Preu, "Industrially feasible multi-crystalline metal wrap through (MWT) silicon solar cells exceeding 16% efficiency," *Solar Energy Materials & Solar Cells,* vol. 93, pp. 1051-55, 2009.

[18] K. Meyer, H.-J. Krokoszinski, D. Lahmer, T. Wuetherich, M. Dupke, R. Jesswein, J. Lossen, P. Zerrer, and A. Prießner, "Novel MWT cell design on monocrystalline silicon wafers," in *Proceedings of the 25th European Photovoltaic Solar Energy Conference and Exhibition*, Valencia, Spain, 2010, pp. 1774-7.

[19] I. G. Romijn, A. A. Mewe, M. W. P. E. Lamers, E. Kossen, E. E. Bende, and A. W. Weeber, "An overview of mwt cells and evolution to aspire concept: a new integrated mc-si cell and module design for high efficiencies," in *Proceedings of the 23rd European Photovoltaic Solar Energy Conference*, Valencia, Spain, 2008, pp. 1-6.

[20] G. Hahn, "Status of selective emitter technology," in *Proceedings of the 25th European Photovoltaic Solar Energy Conference and Exhibition*, Valencia, Spain, 2010, pp. 1091-6.

[21] U. Jäger, S. Mack, A. Kimmerle, A. Wolf, and R. Preu, "Influence of doping profile of highly doped

regions for selective emitter solar cells," in *Proceedings of the 35th IEEE Photovoltaic Specialists Conference*, Honolulu, Hawaii, USA, 2010.

[22] J. Greulich, U. Jäger, S. Rein, and R. Preu, "A review and comparison of one- and two-dimensional simulations of solar cells featuring selective emitters," *IEEE Journal of Photovoltaics,* vol. PP, pp. 1-9, 2012.

[23] T. Fellmeth, A. Born, A. Kimmerle, F. Clement, D. Biro, and R. Preu, "Recombination at metal-emitter interfaces of front contact technologies for highly efficient silicon solar cells," in *Proceedings of the 1st International Conference on Silicon Photovoltaics*, Freiburg, Germany, 2011, pp. 115-21.

[24] D. E. Kane and R. M. Swanson, "Measurement of the emitter saturation current by a contactless photoconductivity decay method (silicon solar cells)," in *Proceedings of the 18th IEEE Photovoltaic Specialists Conference*, Las Vegas, Nevada, USA, 1985, pp. 578-83.

[25] A. L. Fahrenbruch and R. H. Bube, *Fundamentals of solar cells*. New York: Academic Press, 1983.

[26] J. Krause, R. Woehl, and D. Biro, "Analysis of local Al-p^+ -layers for solar cells processed by small screen-printed structures," in *Proceedings of the 25th European Photovoltaic Solar Energy Conference and Exhibition*, Valencia, Spain, 2010, pp. 1899-1904.

[27] K. Bothe, R. Hezel, and J. Schmidt, "Recombination-enhanced formation of the metastable boron-oxygen complex in crystalline silicon," *Applied Physics Letters,* vol. 83, pp. 1125-7, 2003.

[28] K. R. McIntosh, "Lumps, humps and bumps: Three detrimental effects in the current-voltage curve of silicon solar cells," Dissertation, Centre for Photovoltaic Engineering, University of New South Wales, Sydney, Australia, 2001.

[29] R. A. Sinton and A. Cuevas, "A quasi-steady-state open-circuit voltage method for solar cell characterization," in *Proceedings of the 16th European Photovoltaic Solar Energy Conference*, Glasgow, UK, 2000, pp. 1152-5.

[30] A. Nussbaum, "Generation-recombination characteristic behaviour of silicon diodes," *Physica Status Solidi A,* vol. 19, pp. 441-50, 1973.

[31] A. Schenk and U. Krumbein, "Coupled defect-level recombination: Theory and application to anomalous diode characteristics," *Journal of Applied Physics,* vol. 78, pp. 3185-92, 1995.

[32] O. Breitenstein, J. Bauer, A. Lotnyk, and J.-M. Wagner, "Defect induced non-ideal dark I-V characteristics of solar cells," *Superlattices and Microstructures,* vol. 45, pp. 182-9, 2008.

[33] B. T. Michl, M. Rüdiger, J. A. Giesecke, M. Hermle, W. Warta, and M. C. Schubert, "From injection dependent lifetime to solar cell efficiency," in *Proceedings of the 26th European Photovoltaic Solar Energy Conference and Exhibition*, Hamburg, Germany, 2011, pp. 1058-62.

[34] S. R. Wenham, S. J. Robinson, X. Dai, J. Zhao, A. Wang, Y. H. Tang, A. Ebong, C. B. Honsberg, and M. A. Green, "Rear surface effects in high efficiency silicon solar cells," in *Proceedings of the 1st World Conference on Photovoltaic Energy Conversion*, Hawaii, USA, 1994, pp. 2402, 1278-82.

[35] J. Bartsch, A. Mondon, B.-J. Godejohann, M. Hörteis, and S. W. Glunz "Advanced front side metallization for crystalline silicon solar cells based on a fully plated contact," in *Proceedings of the 25th European Photovoltaic Solar Energy Conference and Exhibition*, Valencia, Spain, 2010, pp. 1978-83.

[36] G. Masetti, M. Severi, and S. Solmi, "Modeling of carrier mobility against carrier concentration in arsenic-doped, phosphorus-doped, and boron-doped silicon," *Ieee Transactions on Electron Devices,* vol. 30, pp. 764-769, 1983 1983.

[37] B. Fischer, "Loss analysis of crystalline silicon solar cells using photoconductance and quantum efficiency measurements," Dissertation, Fachbereich Physik, Universität Konstanz, Konstanz, 2003.

[38] B. Thaidigsmann, A. Wolf, and D. Biro, "Accurate determination of the IQE of screen printed silicon solar cells by accounting for the finite reflectance of metal contacts," in *Proceedings of the 24th European Photovoltaic Solar Energy Conference*, Hamburg, Germany, 2009, pp. 2056-9.

[39] U. Jäger, B. Thaidigsmann, M. Okanovic, and R. Preu, "Quantum efficiency analysis of highly doped areas form selective emitter solar cells," in *Proceedings of the 1st International Conference on Silicon Photovoltaics*, Freiburg, Germany, 2011, pp. 193-9.

[40] D. A. Clugston and P. A. Basore, "Modelling free-carrier absorption in solar cells," *Progress in Photovoltaics: Research and Applications,* vol. 5, pp. 229-36, 1997.

[41] A. Cuevas and S. Lopez-Romero, "The combined effect of non-uniform illumination and series resistance on the open-circuit voltage of solar cells. ," *Solar Cells*, vol. 1984, pp. 163-73, 1984.

[42] J. Greulich, M. Glatthaar, A. Krieg, G. Emanuel, and S. Rein, "JV characteristics of industrial silicon solar cells: influence of distributed series resistance and shockley read hall recombination," in *Proceedings of the 24th European Photovoltaic Solar Energy Conference*, Hamburg, Germany, 2009, pp. 2065-9.

[43] H. H. Berger, "Contact resistance and contact resistivity," *Journal of the Electrochemical Society*, vol. 119, pp. 507-14, 1972.

[44] J. M. Gee, W. K. Schubert, and P. A. Basore, "Emitter wrap-through solar cell," in *Proceedings of the 23rd IEEE Photovoltaic Specialists Conference*, Louisville, Kentucky, USA, 1993, pp. 265-70.

[45] R. N. Hall and T. J. Soltys, "Polka Dot Solar Cell," in *Proceedings of the 14th IEEE Photovoltaic Specialists Conference*, San Diego, California, USA, 1980, pp. 550-3.

[46] A. Fallisch and D. Biro, "2-D SPICE simulation and analytical calculation of spreading resistance effects in emitter wrap-through cells with nonsquare via-hole pattern," *IEEE Journal of Photovoltaics*, vol. 1, pp. 153-8, 2011.